
Looking for Tiny Defects via Forward–Backward Feature Transfer

Alex Costanzino
University of Bologna
alex.costanzino@unibo.it

Pierluigi Zama Ramirez
University of Bologna
pierluigi.zama@unibo.it

Giuseppe Lisanti
University of Bologna
giuseppe.lisanti@unibo.it

Luigi Di Stefano
University of Bologna
luigi.distefano@unibo.it

Abstract

Motivated by efficiency requirements, most anomaly detection and segmentation (AD&S) methods focus on processing low-resolution images, e.g., 224×224 pixels, obtained by downsampling the original input images. In this setting, downsampling is typically applied also to the provided ground-truth defect masks. Yet, as numerous industrial applications demand identification of both large and tiny defects, the above-described protocol may fall short in providing a realistic picture of the actual performance attainable by current methods. Hence, in this work, we introduce a novel benchmark that evaluates methods on the original, high-resolution image and ground-truth masks, focusing on segmentation performance as a function of the size of anomalies. Our benchmark includes a metric that captures robustness with respect to defect size, i.e., the ability of a method to preserve good localization from large anomalies to tiny ones. Furthermore, we introduce an AD&S approach based on a novel Teacher–Student paradigm which relies on two shallow MLPs (the Students) that learn to transfer patch features across the layers of a frozen vision transformer (the Teacher). By means of our benchmark, we evaluate our proposal and other recent AD&S methods on high-resolution inputs containing large and tiny defects. Our proposal features the highest robustness to defect size, runs at the fastest speed, yields state-of-the-art performance on the MVTEC AD dataset and state-of-the-art segmentation performance on the VisA dataset.

1 Introduction

Image-based Anomaly Detection and Segmentation (AD&S) aims to identify anomalous samples and localize their defects. This task is particularly challenging in industrial applications where anomalies are varied and unpredictable, and nominal samples may be scarce. In these settings, AD&S is usually tackled in a *cold-start* fashion: the training procedure is unsupervised, with the train set comprising only images of nominal samples. Modern approaches for AD&S [1, 8, 10, 14, 17, 25, 27, 29] create a model of the nominal samples during training, while at inference time each test sample is compared to this nominal model and any discrepancy is interpreted as an anomaly. To reduce both training and inference time, and limit memory occupancy, most of these AD&S solutions create models based on low-resolution images obtained by downsampling the original input images. However, this approach is detrimental to the task since tiny anomalies could be lost due to strong downsampling, as may be observed in Fig. 1. Moreover, it is common practice to downsample also the ground-truth defect masks provided with the benchmarks. Accordingly, as shown in Fig. 1, the areas of defects get smaller, and tiny anomalies may even disappear from the ground-truth. Yet, since many industrial applications require the detection of both large and tiny defects, the practice described above might not accurately reflect the ability of current methods to localize defects of all sizes. Recently, EfficientAD [1] proposed a benchmark in which all the considered methods’ outputs are upsampled to the original ground-truth resolution, although all methods still process a low-resolution input.

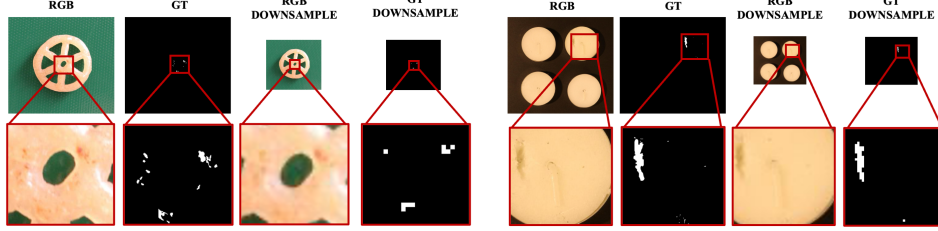


Figure 1: **Effects of downsampling on VisA.** Tiny defects are no longer visible in both RGB and GT.

In this work, we introduce a novel benchmark, referred to as *Tiny Anomalies* where all methods are evaluated on the original ground-truth resolution and, unlike [1], process high-resolution input images. Our benchmark focuses on evaluating segmentation performance as a function of the size of the anomalies and includes a novel metric that captures robustness with respect to the defect size, i.e., the ability to preserve localization performance from large anomalies to tiny ones.

Furthermore, we propose a novel unsupervised AD&S approach that can process high-resolution input images at an exceedingly fast speed. Our approach relies on a frozen transformer backbone [22] and a novel Teacher–Student paradigm whereby lightweight MLPs (i.e., the Students) shared across all patch embeddings learn to mimic the transformation occurring between the layers of the transformer backbone (i.e., the Teacher) by observing only nominal samples. At inference time, for each patch, the actual features computed by the teacher are compared to those predicted by the students, with the discrepancies between the former and the latter highlighting the presence of anomalies.

The strengths of our method come from several reasons. As far as the representation of small defects is concerned, a transformer backbone can effectively handle high-resolution inputs because, although it processes images by dividing them into patches, which results in a lower spatial size, the input information is not compressed, on the contrary, each patch is expanded to a higher dimensionality related to the internal representation of the transformer (e.g. RGB patches of $14 \times 14 \times 3$ pixels are mapped into 768-dimensional embeddings in [22]). These features undergo subsequent transformations, through the different layers of the transformer, which further enrich the representation by increasing their level of contextualization. In particular, we rely on DINO-v2 [22] which has been trained on images of varying resolutions. For what concerns computational requirements, each of these rich, highly contextualized feature vectors can be processed independently through shared shallow MLPs which permits extremely fast batched processing.

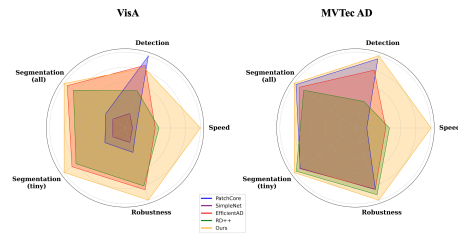


Figure 2: **Comparison between AD&S methods by the Tiny Anomalies benchmark.** The metrics reported in the charts are described in Sec. 4. Values are normalized for better readability.

As depicted in Fig. 2, our approach achieves the best segmentation performance on all defects, including tiny ones, demonstrates superior robustness, and is significantly faster than other methods. Our contribution can be summarized as follows: (i) we propose an evaluation protocol to establish a common ground, enabling comparison of performance across different AD&S methods; (ii) we introduce a novel benchmark to assess how effectively AD&S methods handle tiny anomalies; (iii) we propose a novel AD&S method that exhibits state-of-the-art performance on MVTec AD and state-of-the-art segmentation performance on VisA, while running at a remarkably higher speed than all competitors; (iv) our proposal achieves state-of-the-art segmentation performance on a challenging few-shot AD benchmark built upon the VisA dataset.

2 Related work

Anomaly detection benchmarks. During the last few years, several AD&S datasets have been released. The introduction of MVTec AD [4] kicked off the development of AD&S approaches for industrial applications. This dataset contains several industrial inspection scenarios, each comprising

both train and test sets. Each train set contains only nominal images, while the test sets also contain anomalous samples. Such scenario represents realistic real-world applications where types and possible locations of defects are unknown during the development of AD&S algorithms. Later, the work was extended with the MVTEC 3D-AD [6] dataset, which follows the same structure of MVTEC AD, but also provides the pixel-aligned point clouds of the samples to address the AD&S in a multimodal fashion. Shortly afterwards the Eyecandies [7] dataset was released, which mimics the structure of MVTEC 3D-AD by introducing a multimodal synthetic dataset containing images, point clouds and normals for each sample. To provide a more challenging scenario the VisA dataset [34] has been introduced, in which high-resolution images of complex scenes that can also contain multiple instances of the same object has been released. In the end, more task-specific datasets such as MAD [33] and MVTEC LOCO [3] have been released. In particular, MAD [33] introduced a multi-pose dataset with images from different viewpoints covering a wide range of poses to tackle a pose-agnostic AD&S. MVTEC LOCO [3] not only contains structural anomalies, such as dents or holes but also logical anomalies, which violations of logical constraints can be for instance a wrong ordering or a wrong combination of normal objects.

Anomaly detection solutions. Several approaches have been proposed in the literature to perform AD&S. These solutions can be categorized based on the approach followed to model nominal samples. Normalizing Flows [10, 17, 23, 26, 32] based methods construct complex distributions by transforming a probability density via a series of invertible mappings. In particular, these methods extract features of normal images from a pre-trained model and transform the feature distribution into a Gaussian distribution during the training phase. At test time, after passing the extracted features through the Normalizing Flow, the features of abnormal images will deviate from the Gaussian distribution of the training phase, suggesting an anomaly. Lately, several solutions [2, 11, 25] that employ Memory Banks have been introduced. This category of solutions exploits well-known feature extractors trained on a large plethora of data [9, 18, 22] to model nominal samples. More in detail, during training, the feature extractor is kept frozen and used to compute features for nominal samples which are then stored in a memory bank. At test time, the features extracted from an input image are compared to those in the bank in order to identify anomalies. Despite their remarkable performance, these approaches suffer from slow inference speed, since each feature vector extracted from the input image needs to be compared against all the nominal feature vectors stored in the memory bank. Methods close to our solution which follows a Teacher–Student strategy [1, 5, 8, 14, 28, 29, 31] have also been proposed. In this family of solutions, the training phase involves a teacher model that extracts features from nominal samples and distills this knowledge to the student model, which learns to mimic the teacher’s feature extraction process. During the testing phase, differences between the features generated by the teacher model and those produced by the student model reveal the presence of anomalies. Recently, a multimodal approach [12] investigated the idea of mapping features from one modality to the other on nominal samples and then detecting anomalies by pinpointing inconsistencies between observed and mapped features. This solution leverages MLPs to learn a mapping between features coming from two different modalities, RGB images and point clouds. Differently, our solution does not necessarily require two modalities but can pinpoint anomalies by looking for discrepancies between extracted and transferred features of the same modality.

3 Method

As outlined in Fig. 3, our approach follows a Teacher–Student paradigm in which the Teacher, \mathcal{T} , is represented by a frozen transformer encoder [22] while we define two students, referred to as Forward and Backward Transfer Network (\mathcal{S}_F and \mathcal{S}_B) realized as shallow MLPs.

The Students are trained on nominal samples and learn to mimic the transformations between the patch embeddings occurring within the layers of the Teacher. In particular, the Forward Transfer Network learns to predict the patch embeddings computed by a layer of the transformer (k in Fig. 3), given the corresponding embeddings computed by a previous layer (j in Fig. 3). Conversely, the Backward Transfer Network learns to predict the features calculated by the transformer at layer j given the corresponding ones at layer k . The Student networks \mathcal{S}_F , \mathcal{S}_B are shared across patch embeddings, i.e., both take as input the features associated with the patch (i) at a layer $f_j^{(i)}$, $f_k^{(i)}$ and predict the corresponding features at the other layer $\hat{f}_k^{(i)}$, $\hat{f}_j^{(i)}$. At inference time, for all patch embeddings of the given test sample, the features predicted by the Students are compared to the ones

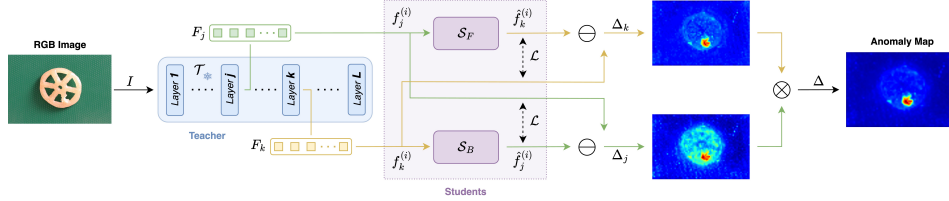


Figure 3: **Proposed method.** Given an RGB Image I , a frozen pre-trained transformer backbone \mathcal{T} is leveraged to extract two sets of patch-aligned features F_j, F_k , from different layers, one from a lower contextualization layer j and one from a higher contextualization layer k . Then, a pair of feature transfer networks, $\mathcal{S}_F, \mathcal{S}_B$, predict the extracted features from one layer to the other, processing the features at each patch independently. Lastly, extracted and transferred features are compared through a Euclidean distance, to create contextualization-specific anomaly maps, Δ_j, Δ_k , that are then combined to obtain the final anomaly map Δ .

extracted by the Teacher, with the discrepancies between the former and the latter providing the signal to highlight anomalies. In particular, as shown in Fig. 3, the difference between the outputs from $\mathcal{S}_F, \mathcal{S}_B$ and the actual patch embeddings from layers k, j of \mathcal{T} yield two anomaly maps, Δ_j and Δ_k , that are fused to obtain the final one. Due to the key novelty of our AD&S approach relying on the novel pretext task realized through $\mathcal{S}_F, \mathcal{S}_B$, we dub it Forward Backward Feature Transfer (FBFT).

The intuition behind our approach relies on the observation that as patch embeddings travel from shallower to deeper layers of a transformer encoder they become more and more contextualized, i.e., deeper representations capture more global information that helps singling out a patch based on the specific context provided by the input image. This complex contextualization function is performed progressively through the layers, with the different attention heads specializing in performing different tasks [30]. Hence, our Forward and Backward Transfer networks are trained to contextualize and de-contextualize patch embeddings according to the function, which we assume to be invertible, executed by the transformer between a pair of chosen layers. We conjecture that feature contextualization and de-contextualization are complex functions that do not admit a trivial solution, such as, e.g., the identity. Therefore, small-capacity networks trained only on nominal samples are unlikely to learn general functions that can yield correct predictions on out-of-distribution data, i.e. features extracted from anomalous patches. In the following, we provide additional details on our AD&S pipeline.

Teacher. As a first step, we provide as input to the teacher \mathcal{T} an image I with dimensions $H \times W \times C$, where H, W , and C correspond to the height, width, and number of channels. In our framework, we employ a Transformer-based backbone that provides after each layer a set of features, one for each input patch processed by the backbone. Each feature, $f^{(i)} \in \mathbb{R}^D$, has dimension D according to the inner representation employed by the backbone, while the number of features is $N = HW/P^2$, where the patch size is $P \times P$ pixels. During the forward pass, we extract two sets of features, $F_j = \{f_j^{(i)}, i = 1 \dots N\}$ and $F_k = \{f_k^{(i)}, i = 1 \dots N\}$, from two different layers of the backbone, i.e. layers j and k , with $j < k$.

Students. The two sets of features extracted by the Teacher are processed by a pair of Forward and Backward Transfer networks, \mathcal{S}_F and \mathcal{S}_B , which in our architecture represent the students. \mathcal{S}_F maps a feature vector from a less contextualized layer j to a more contextualized layer k , while \mathcal{S}_B does the opposite. Each network predicts the features of one layer from the corresponding ones extracted from the other, processing each patch location independently. Thus, given a patch location (i) and the corresponding features $f_j^{(i)}$ and $f_k^{(i)}$, the features predicted by the students can be expressed as:

$$\hat{f}_k^{(i)} = \mathcal{S}_F(f_j^{(i)}) \quad \hat{f}_j^{(i)} = \mathcal{S}_B(f_k^{(i)}) \quad (1)$$

where \mathcal{S}_F and \mathcal{S}_B are parametrized as MLPs, shared across all patches. By processing all patches, we obtain the two sets of transferred features: $\hat{F}_j = \{\hat{f}_j^{(i)}, i = 1 \dots N\}$ and $\hat{F}_k = \{\hat{f}_k^{(i)}, i = 1 \dots N\}$.

Training. During training, the weights of \mathcal{S}_F and \mathcal{S}_B are optimized considering only images of nominal samples of a specific class from a dataset. As loss function, for both networks we employ

the cosine distance between the features extracted from the backbone at the considered layers and the transferred ones. Thus, the per-patch losses are:

$$\mathcal{L}_j^{(i)}(f_j^{(i)}, \hat{f}_j^{(i)}) = 1 - \frac{f_j^{(i)} \cdot \hat{f}_j^{(i)}}{\|f_j^{(i)}\| \|\hat{f}_j^{(i)}\|} \quad \mathcal{L}_k^{(i)}(f_k^{(i)}, \hat{f}_k^{(i)}) = 1 - \frac{f_k^{(i)} \cdot \hat{f}_k^{(i)}}{\|f_k^{(i)}\| \|\hat{f}_k^{(i)}\|} \quad (2)$$

Inference. At inference time, the image under analysis is processed by the transformer backbone and the features extracted from the two layers, F_j and F_k are provided as input to the Forward and Backward Transfer networks to obtain the corresponding transferred features, \hat{F}_j and \hat{F}_k . The Euclidean distance is then employed to compute the patch-wise differences between extracted and transferred features $\Delta_j^{(i)}, \Delta_k^{(i)}$:

$$\Delta_j^{(i)} = \|f_j^{(i)} - \hat{f}_j^{(i)}\|_2 \quad \Delta_k^{(i)} = \|f_k^{(i)} - \hat{f}_k^{(i)}\|_2, \quad i = 1 \dots N \quad (3)$$

which are then fused by multiplying those corresponding to the same patch:

$$\Delta^{(i)} = \Delta_j^{(i)} \cdot \Delta_k^{(i)}, \quad i = 1 \dots N \quad (4)$$

The set of fused differences, $\Delta^{(i)}$, is reshaped as a $\sqrt{N} \times \sqrt{N}$ anomaly map according to the positions of the patches within the input image. This map is then up-sampled to $H \times W$, i.e. the spatial size of the input image, by bilinear interpolation and successively smoothed according to common practice [12, 21, 25, 29]. The global anomaly score required to perform sample-level anomaly detection is computed as the mean value of the top M values of the final anomaly map Δ .

4 Tiny Anomalies benchmark

Most of the existing AD&S proposals operate on downsampled versions of the images, mainly due to computational constraints. However, as highlighted in Sec. 1 this practice is detrimental for tiny defects which tend to be reduced or in the worst case disappear in the downsampled versions of the input image and the ground truth. To this end, we introduce a cumulative quartile-based benchmark designed to analyze AD&S performance across defects of varying sizes.

Datasets. To define such a benchmark we rely on two AD&S datasets: VisA [34] and MVTec AD [4]. The VisA [34] dataset provides images of varying resolution, with the height spanning from 1284 to 1562 pixels and anomalies as tiny as 1 pixel and up to 478781 pixels.

The dataset contains 10821 images of 12 objects across 3 domains, with challenging scenarios including complex structures in objects, multiple instances, and pose variations. Between the provided images, 9621 are nominals while 1200 contains defects. The MVTec AD dataset mimics real-world industrial inspection scenarios and includes 5354 images, with heights spanning from 700 to 1024 pixels and anomalies ranging from 24 pixels to 517163 pixels. The images pertain to 15 objects exhibiting 73 different types of anomalies for 1888 anomalous samples.

Both VisA and MVTec AD provide pixel-accurate ground truths for each anomalous sample to allow us to evaluate methods on both anomaly classification and segmentation. As highlighted in Fig. 4, VisA features a significantly wider range of anomaly sizes and includes tiny defects. As a result, downsampling the ground-truths to 224×224 pixels, i.e., the most commonly employed inference and evaluation size in present literature, yields a reduction in the number of defects of 21.42% and 0.37% for VisA and MVTec AD, respectively.

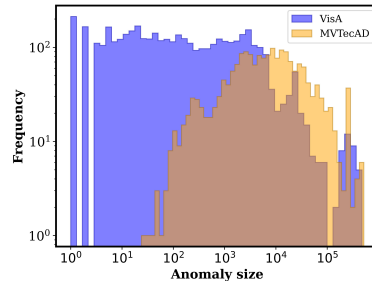


Figure 4: **Anomaly size distribution.**

4.1 Metrics.

The metrics defined in our benchmark build upon the evaluation proposed by MVTec AD [4] and VisA [34]. These two datasets, assess the image anomaly detection performance employing the Area

Under the Receiver Operator Curve (I-AUROC) computed on the global anomaly score. As for segmentation performance, the Area Under the Per-Region Overlap (AUPRO) on the anomaly map is computed, with the integration threshold set to 0.3. Recently, [1, 12] have proposed to compute the AUPRO considering a tighter threshold, i.e., 0.05. We will consider both metrics and denote AUPROs with integration thresholds 0.3 and 0.05 as AUPRO@30%, and AUPRO@5%, respectively.

Performance across defects sizes. To highlight the capability of each method to segment defects with varying sizes, in our novel benchmark, we introduce a variation of the AUPRO metric. In particular, for each object in a dataset, we compute the anomaly size distribution and partition it in cumulative quartiles, denoted as Q_1, Q_2, Q_3, Q_4 . These cumulative quartiles are associated with sets that contain only anomalies with a size smaller than or equal to the considered quartile. Hence, the set associated with Q4 consists of all anomalies, while Q1 includes only the smallest ones. Then, we calculate the AUPRO@30% and AUPRO@5% on each set, with the segmentation metrics associated with Q4 being the already described segmentation metrics adopted in current benchmarks.

Robustness. We introduce a novel metric, ρ , aimed at assessing the robustness of a method w.r.t. the size of the defects in a dataset. In particular, ρ captures the ability of a method to segment accurately tiny defects as well as larger ones. Accordingly, we define the robustness as:

$$\rho = w \cdot (1 - s), \quad s = \frac{|\text{AUPRO}(Q_4) - \text{AUPRO}(Q_1)|}{\max(\text{AUPRO}(Q_1), \text{AUPRO}(Q_4))}, \quad w = \frac{1}{4} \cdot \sum_{i=1}^4 \text{AUPRO}(Q_i) \quad (5)$$

Here, for the sake of compactness, we denote as AUPRO either AUPRO@5% or AUPRO@30%, such that considering the former or the latter will yield $\rho@5\%$ or $\rho@30\%$, respectively. In the definition of ρ , the AUPRO is evaluated for the smallest defects only, i.e., $\text{AUPRO}(Q_1)$, and for all defects, i.e., $\text{AUPRO}(Q_4)$. With this measure, if a method can correctly segment larger defects but struggles with small ones, its sensitivity to defect size, s , is high and its robustness, ρ , is low. Conversely, a robust method should be able to accurately segment defects regardless of their sizes, which in our metric would be captured by the difference between $\text{AUPRO}(Q_4)$ and $\text{AUPRO}(Q_1)$ turning out low, yielding low sensitivity and high robustness. Yet, to avoid deeming as robust a method that performs poorly on both small and large defects, such that $\text{AUPRO}(Q_4)$ and $\text{AUPRO}(Q_1)$ are both similarly low, we propose to introduce the average AUPRO across all quartiles, denoted as w , as weighing factor of the term $(1 - s)$ in the definition of ρ . It is worth pointing out that the proposed robustness metric, ρ , is bounded by 1 since both s and w are smaller than 1.

We dub our benchmark *Tiny Anomalies* and define as its main metrics: (i) I-AUROC, (ii) AUPRO@5%, (iii) AUPRO@5%(Q_1), (iv) $\rho@5\%$ and (v) inference time in ms. These main metrics are reported in Fig. 2, where they are referred to as (i) Detection, (ii) Segmentation (all), (iii) Segmentation (tiny), (iv) Robustness and (v) Speed. Nonetheless, in Sec. 5, we provide also the standard segmentation metrics based on AUPRO@30% for both VisA and MVTec AD.

4.2 Evaluation protocol

We evaluate our proposal, FBFT, alongside with several state-of-the-art AD&S methods, such as PatchCore [25], SimpleNet [21], EfficientAD [1] and RD++ [29]. As our benchmark emphasizes the ability to deal with tiny anomalies, we provide as input to all methods images at the highest resolution that would enable execution on a single GPU, so as to avoid or minimize downsampling. In particular, we could handle input images up to 1036×1036 pixels with EfficientAD, RD++ and FBFT, while the highest input resolution for PatchCore and SimpleNet was found to be 512×512 pixels.

As described in [1], the results reported in SimpleNet [21] are obtained by repeatedly evaluating the metrics on all test images during training to select the best check-point. Analyzing the official implementation, we noticed how this protocol has been followed also by RD++ [29]. However, in real-world settings, the test data is not available at training time. Thus, to avoid overestimating the actual performance of the models, we disable the above check-point selection mechanism, train all methods for a fixed number of epochs and evaluate the model obtained at the last checkpoint. For [1, 21, 29], we train for the number of epochs specified in the official implementations.

PatchCore [25] employs a centre-crop of the input images since in MVTec AD, most of the defects lie within this cropped area. However, in a real-world scenario, anomalies can occur outside of this area, thus, we disable this strategy as it implies knowledge about the location of anomalies in the test set.

As anticipated in Sec. 1, we compute all metrics based on the original ground-truths provided with the datasets, which have the same resolution as the original input images. Hence, we do not downsample the ground-truths to the input image size processed by a method. If a method outputs an anomaly map at a smaller resolution than the original ground-truth, we bilinearly upsample the anomaly map to the same resolution as the ground-truth in order to calculate all metrics.

Some methods, including ours, must add padding to the input image in order to adapt it to the input size of the employed backbone. However, we remove these extra pixels from the final anomaly maps as, otherwise, they usually decrease the False Positive Rate (and thus artificially ameliorate the segmentation metrics) because they tend to yield very low anomaly scores. Finally, we calculate the AUPRO considering all the samples in the test set, both nominal and anomalous¹.

5 Experiments

Implementation details. EfficientAD [1] proposes two variants: EfficientAD-S and EfficientAD-M. We consider the latter since it provides better AD&S performance. To implement our Feature Extractor we employ DINO-v2 ViT-B/14 [22] pre-trained on a large, curated and diverse dataset of 142 million images, comprising ImageNet-22k [15, 24]. Thus, \mathcal{T} processes $1036 \times 1036 \times 3$ RGB images and outputs $74 \times 74 \times 768$ feature maps. Both \mathcal{S}_F and \mathcal{S}_B consist of three linear layers, each but the last one followed by GeLU activations. The number of units per layer is 768 for both \mathcal{S}_F and \mathcal{S}_B . The two networks are trained jointly for 50 epochs using Adam [20] with a learning rate of 0.001. We select the layers $j = 8$ and $k = 12$ to realize the Feature Transfer Networks. A detailed ablation study on the choice of the best pair of layers is reported in the supplemental material. We employed $M = 0.001 \cdot H \cdot W$ to attain the number of pixels used to calculate the global anomaly score. We conducted all the experiments on a single NVIDIA GeForce RTX 4090.

Anomaly detection and segmentation. Following the proposed evaluation protocol, described in Sec. 4, we evaluate our method on VisA and MVTec AD, reporting the results in Tab. 1. Our approach achieves the best segmentation results on the VisA dataset, with 0.952 AUPRO@30% and 0.787 AUPRO@5% and the state-of-the-art in both detection and segmentation on the MVTec AD dataset, with 0.988 I-AUROC, 0.945 AUPRO@30%, and 0.782 AUPRO@5%. Regarding detection performance on VisA, our method attains results comparable to the runner-up (0.968 of EfficientAD vs. 0.964 of Ours). The supplemental material provides the detailed per-class metrics for each method. In Fig. 5, we depict some qualitative results on the VisA dataset. Our method provides

Table 1: **I-AUROC, AUPRO30@% and AUPRO5@% on VisA and MVTec AD for several AD&S methods.** Average metrics of all classes on the respective test set. Best results in **bold**, runner-ups underlined. All methods are trained and tested at high resolution.

Algorithm	VisA			MVTec AD		
	I-AUROC	AUPRO@30%	AUPRO@5%	I-AUROC	AUPRO@30%	AUPRO@5%
PatchCore [25]	0.982	0.752	0.542	<u>0.983</u>	<u>0.937</u>	0.701
SimpleNet [21]	0.904	0.718	0.469	–	–	–
EfficientAD [1]	<u>0.968</u>	<u>0.937</u>	<u>0.777</u>	0.965	0.920	<u>0.757</u>
RD++ [29]	0.930	0.907	0.758	0.915	0.901	0.716
FBFT (Ours)	0.964	0.952	0.787	0.988	0.945	0.782

more localized anomaly scores compared to EfficientAD [1], i.e., the second-best method on VisA. For instance, by looking at the *capsules* example, our anomaly score peak is centered on the anomaly differently from [1]. Further qualitative results are reported in the supplemental material.

Cumulative quartiles based anomaly segmentation. We report in Tab. 2 the analysis on VisA and MVTec AD of the performance w.r.t. anomaly size using the cumulative quartile metrics defined in Sec. 4. The results highlight that the defect size impacts the segmentation metrics, especially for the tiniest ones, i.e., the anomalies in Q_1 . Nevertheless, our method is the best across all quartiles, with a notable gap compared to the second-best method on Q_1 on VisA, which is the dataset with the highest frequency of tiny defects (e.g., AUPRO30@% 0.935 Ours vs. 0.890 EfficientAD). Additionally, our

¹We noticed that official code from [25], calculates the AUPRO only on anomalous test samples, obtaining higher scores since the false positive rate is inherently lower with this protocol.

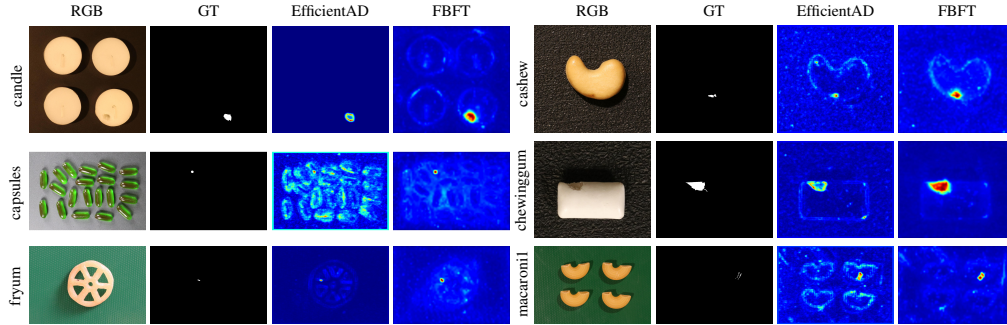


Figure 5: **VisA dataset qualitative results.** All methods are trained and tested at high resolution.

method is remarkably stable and robust across quartiles. For instance, on VisA, we go from 0.758 to 0.730 AUPRO5@%, losing only 2.6% segmentation quality, remarkably less than the runner-up method, EfficientAD, which decreases its performance of 6.7%, from 0.743 to 0.693 AUPRO5@%.

Table 2: **Quartile-based benchmark.** Best results in **bold**, runner-ups underlined.

Algorithm	Dataset	AUPRO@30%						AUPRO@5%					
		Q_1	Q_2	Q_3	Q_4	\bar{Q}	$\rho@30\%$	Q_1	Q_2	Q_3	Q_4	\bar{Q}	$\rho@5\%$
PatchCore [25]	VisA	0.703	0.720	0.740	0.752	0.728	0.679	0.484	0.492	0.518	0.542	0.509	0.454
SimpleNet [21]		0.658	0.668	0.696	0.718	0.685	0.627	0.390	0.399	0.435	0.469	0.423	0.351
EfficientAD [1]		0.890	0.923	0.933	0.937	0.920	0.873	0.693	0.741	0.763	0.777	0.743	0.662
RD++ [29]		0.867	0.898	0.906	0.907	0.894	0.853	0.710	0.740	0.755	0.758	0.740	0.692
FBFT (Ours)		0.935	0.941	0.946	0.952	0.943	0.926	0.730	0.749	0.768	0.787	0.758	0.702
PatchCore [25]	MVTec AD	0.924	0.932	0.935	0.937	0.932	0.918	0.653	0.677	0.691	0.701	0.680	0.633
EfficientAD [1]		0.922	0.925	0.925	0.920	0.923	0.920	0.758	0.769	0.767	0.757	0.762	0.760
RD++ [29]		0.946	0.922	0.918	0.901	0.921	0.952	0.782	0.752	0.744	0.716	0.748	0.684
FBFT (Ours)		0.958	0.948	0.947	0.945	0.949	0.986	0.806	0.798	0.795	0.782	0.795	0.783

Inference time. We report in Tab. 3 the inference time and main AD&S metrics on VisA for our method and state-of-the-art approaches [1, 21, 25, 29]. Using the same machine, we compute the speed in ms per sample as the average across all the test samples of the VisA dataset. For each method, we compute the inference time, from when the sample is available on the GPU to the computation of the anomaly scores, after a GPU warm-up, synchronizing all threads before estimating the total inference time. Our approach attains state-of-the-art anomaly segmentation performance, namely AUPRO@30%, $\rho@30\%$, AUPRO@5%, and $\rho@5\%$, while being extremely fast. We highlight that, even though PatchCore attains the best detection performance on the VisA dataset, it largely falls behind in terms of segmentation performance (AUPRO@30%=0.752 of PatchCore vs. AUPRO@30%=0.952 of Ours, AUPRO@5%=0.542 of PatchCore vs. AUPRO@5%=0.787 of Ours), and inference speed (227.230 ms of PatchCore vs. 1.786 ms of Ours).

Table 3: **Inference speed and AD performance on VisA dataset.** Inference Time in ms per sample. Best results in **bold**, runner-ups underlined. All methods are trained and tested at high-resolution.

Algorithm	Inference Time	I-AUROC	AUPRO@30%	$\rho@30\%$	AUPRO@5%	$\rho@5\%$
PatchCore [25]	227.230	0.982	0.752	0.679	0.542	0.454
SimpleNet [21]	560.617	0.896	0.718	0.627	0.469	0.351
EfficientAD [1]	82.367	<u>0.968</u>	<u>0.937</u>	<u>0.873</u>	<u>0.777</u>	0.662
RD++ [29]	63.176	0.930	0.907	0.853	0.758	<u>0.692</u>
FBFT (Ours)	1.786	0.964	0.952	0.926	0.787	0.702

Few-shot anomaly detection and segmentation. As mentioned in Sec. 1, collecting many nominal samples in most industrial scenarios can be extremely expensive or unfeasible. Also, frequent production changeover requires fast adaptation. For these reasons, a beneficial property of AD&S methods is the ability to create a model of the nominal data even with few samples. We define a few-shot benchmark – based on the VisA dataset – randomly selecting 5, 10, and 50 images from each category as training data. We train the compared methods [1, 21, 25, 29] along with our proposed

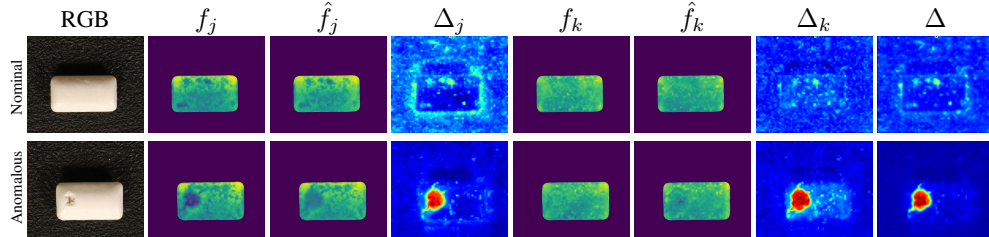


Figure 6: **Features visualization.** Channels average of feature maps before and after feature mapping.

approach on these samples, and we test them on the entire test set, with the evaluation protocol proposed in Sec. 4, reporting the results in Tab. 4. We obtain the best segmentation performance for both metrics (AUPRO@30% and AUPRO@5%) in all the few-shot settings, significantly improving the most challenging segmentation metrics (+0.167 AUPRO@5% on 5-shot) and retaining a stable segmentation performance (AUPRO@30% always above 0.9) across the various settings. These results confirm the ability of our method to optimize feature transfer networks even from a few nominal samples, thanks to the patch-independent processing enabled by the MLPs.

Table 4: **Few-shot AD&S performance.** Best results in **bold**, runner-ups underlined.

Algorithm	Full			50-shot			10-shot			5-shot		
	I-AUROC	AUPRO@30%	AUPRO@5%	I-AUROC	AUPRO@30%	AUPRO@5%	I-AUROC	AUPRO@30%	AUPRO@5%	I-AUROC	AUPRO@30%	AUPRO@5%
PatchCore [25]	0.982	0.752	0.542	0.959	0.724	0.485	0.948	0.704	0.459	0.916	0.698	0.455
SimpleNet [21]	0.896	0.718	0.469	0.917	0.758	0.430	0.883	0.725	0.408	0.862	0.691	0.377
EfficientAD [11]	<u>0.968</u>	<u>0.927</u>	0.777	0.831	<u>0.854</u>	0.569	0.816	<u>0.806</u>	0.469	0.810	0.834	0.511
RD++ [29]	0.930	0.907	0.758	0.776	0.861	0.563	0.615	0.733	0.303	0.555	0.654	0.253
FBFT (Ours)	0.964	0.952	0.787	<u>0.927</u>	0.934	0.743	<u>0.897</u>	0.910	0.695	<u>0.879</u>	0.901	0.678

Features visualization. In Fig. 6, we show the contextualized feature maps before f_j, f_k and after \hat{f}_j, \hat{f}_k the feature transfer, as well as their Δ_j, Δ_k and final anomaly maps Δ , for a nominal (top) and an anomalous (bottom) test sample of VisA. In the nominal case, we can notice how the features before and after the feature transfer look similar, resulting in low anomaly scores. In the anomalous case, as the extracted features f_j, f_k fall out of the nominal distribution, the feature transfer network fails to contextualize or decontextualize them, resulting in erroneously reconstructed features \hat{f}_j and \hat{f}_k . Thus, by analyzing the discrepancy between the original and reconstructed features, we produce accurate anomaly maps. Furthermore, after the combination, the overall anomaly map Δ exhibits less noise, thanks to the product-based aggregation employed in this work.

6 Discussion

We introduced a benchmark to evaluate the stability of existing methods in segmenting anomalies of different sizes, spanning from very tiny to larger ones, along with a fair and sound evaluation protocol to assess the performance. We hope to establish this protocol as a common practice when evaluating AD&S metrics, to standardize results and render methods truly comparable. In addition, we introduced a fast and lightweight approach based on forward-backward transfer networks that process features extracted from layers with different contextualization levels of a transformer backbone. The proposed solution achieves the best segmentation results on the VisA dataset, both on the classical benchmark and the proposed one, while also running at a remarkably faster speed, compared to existing AD&S approaches. Also, it exhibits state-of-the-art performance on the MVTec AD dataset. Lastly, our approach outperforms competitors in segmentation performance also when considering a more challenging few-shot scenario built upon the VisA dataset.

Though transformers can create a rich representation for each patch of the input high-resolution image, a limitation of our method resides in the small spatial size of the output anomaly map, which is constrained by the leveraged backbone and demand bilinear upsampling to the input resolution. An idea to enhance the introduced framework would be to employ strategies that can yield high-resolution feature maps, such as NaViT [13], which, by efficiently performing repeated inference across an image, can output higher-resolution feature maps, or FeatUp [16], which can restore lost spatial information in deep features, yielding feature maps with the same spatial size as the input.

References

- [1] Batzner, K., Heckler, L., König, R.: Efficientad: Accurate visual anomaly detection at millisecond-level latencies. In: Proceedings of the IEEE/CVF Winter Conference on Applications of Computer Vision (WACV). pp. 128–138 (January 2024)
- [2] Bergman, L., Cohen, N., Hoshen, Y.: Deep nearest neighbor anomaly detection. arXiv preprint arXiv:2002.10445 (2020)
- [3] Bergmann, P., Batzner, K., Fauser, M., Sattlegger, D., Steger, C.: Beyond dents and scratches: Logical constraints in unsupervised anomaly detection and localization. *International Journal of Computer Vision* **130** (04 2022). <https://doi.org/10.1007/s11263-022-01578-9>
- [4] Bergmann, P., Fauser, M., Sattlegger, D., Steger, C.: Mvtec ad – a comprehensive real-world dataset for unsupervised anomaly detection. In: Proceedings of the IEEE/CVF Conference on Computer Vision and Pattern Recognition (CVPR) (June 2019)
- [5] Bergmann, P., Fauser, M., Sattlegger, D., Steger, C.: Uninformed students: Student-teacher anomaly detection with discriminative latent embeddings. In: Proceedings of the IEEE/CVF conference on computer vision and pattern recognition. pp. 4183–4192 (2020)
- [6] Bergmann, P., Xin, J., Sattlegger, D., Steger, C.: The mvtec 3d-ad dataset for unsupervised 3d anomaly detection and localization. In: Proceedings of the 17th International Joint Conference on Computer Vision, Imaging and Computer Graphics Theory and Applications. vol. 5: VISAPP, pp. 202–213 (2022). <https://doi.org/DOI:10.5220/0010865000003124>
- [7] Bonfiglioli, L., Toschi, M., Silvestri, D., Fioraio, N., De Gregorio, D.: The eyecandies dataset for unsupervised multimodal anomaly detection and localization. In: Proceedings of the 16th Asian Conference on Computer Vision (ACCV2022 (2022), aCCV
- [8] Cao, Y., Wan, Q., Shen, W., Gao, L.: Informative knowledge distillation for image anomaly segmentation. *Knowledge-Based Systems* **248**, 108846 (2022)
- [9] Caron, M., Touvron, H., Misra, I., Jégou, H., Mairal, J., Bojanowski, P., Joulin, A.: Emerging properties in self-supervised vision transformers. In: Proceedings of the International Conference on Computer Vision (ICCV) (2021)
- [10] Chiu, L.L., Lai, S.H.: Self-supervised normalizing flows for image anomaly detection and localization. In: Proceedings of the IEEE/CVF Conference on Computer Vision and Pattern Recognition. pp. 2926–2935 (2023)
- [11] Cohen, N., Hoshen, Y.: Sub-image anomaly detection with deep pyramid correspondences. ArXiv (2020)
- [12] Costanzino, A., Zama Ramirez, P., Lisanti, G., Di Stefano, L.: Multimodal industrial anomaly detection by crossmodal feature mapping. In: Proceedings of the IEEE Conference on Computer Vision and Pattern Recognition (2024), cVPR
- [13] Dehghani, M., Mustafa, B., Djolonga, J., Heek, J., Minderer, M., Caron, M., Steiner, A.P., Puigcerver, J., Geirhos, R., Alabdulmohsin, I., Oliver, A., Padlewski, P., Gritsenko, A.A., Lucic, M., Houlsby, N.: Patch n’ pack: Navit, a vision transformer for any aspect ratio and resolution. In: Thirty-seventh Conference on Neural Information Processing Systems (2023), <https://openreview.net/forum?id=VpGFHmI7e5>
- [14] Deng, H., Li, X.: Anomaly detection via reverse distillation from one-class embedding. In: Proceedings of the IEEE/CVF Conference on Computer Vision and Pattern Recognition. pp. 9737–9746 (2022)
- [15] Deng, J., Dong, W., Socher, R., Li, L.J., Li, K., Fei-Fei, L.: Imagenet: A large-scale hierarchical image database. In: 2009 IEEE conference on computer vision and pattern recognition. pp. 248–255. Ieee (2009)
- [16] Fu, S., Hamilton, M., Brandt, L.E., Feldmann, A., Zhang, Z., Freeman, W.T.: Featup: A model-agnostic framework for features at any resolution. In: The Twelfth International Conference on Learning Representations (2024), <https://openreview.net/forum?id=GkJiNn2QDF>
- [17] Gudovskiy, D., Ishizaka, S., Kozuka, K.: Cflow-ad: Real-time unsupervised anomaly detection with localization via conditional normalizing flows. In: Proceedings of the IEEE/CVF Winter Conference on Applications of Computer Vision. pp. 98–107 (2022)
- [18] He, K., Chen, X., Xie, S., Li, Y., Dollár, P., Girshick, R.: Masked autoencoders are scalable vision learners. In: Proceedings of the IEEE/CVF conference on computer vision and pattern recognition. pp. 16000–16009 (2022)

- [19] Jelenić, F., Jukić, J., Tutek, M., Puljiz, M., Snajder, J.: Out-of-distribution detection by leveraging between-layer transformation smoothness. In: The Twelfth International Conference on Learning Representations (2024), <https://openreview.net/forum?id=AcRfzLS6se>
- [20] Kingma, D.P., Ba, J.: Adam: A method for stochastic optimization. In: The International Conference on Learning Representations (ICLR) (2015)
- [21] Liu, Z., Zhou, Y., Xu, Y., Wang, Z.: Simplenet: A simple network for image anomaly detection and localization. In: Proceedings of the IEEE/CVF Conference on Computer Vision and Pattern Recognition. pp. 20402–20411 (2023)
- [22] Oquab, M., Darcet, T., Moutakanni, T., Vo, H.V., Szafraniec, M., Khalidov, V., Fernandez, P., Haziza, D., Massa, F., El-Nouby, A., Howes, R., Huang, P.Y., Xu, H., Sharma, V., Li, S.W., Galuba, W., Rabbat, M., Assran, M., Ballas, N., Synnaeve, G., Misra, I., Jegou, H., Mairal, J., Labatut, P., Joulin, A., Bojanowski, P.: DINOv2: Learning robust visual features without supervision (2023)
- [23] Papamakarios, G., Nalisnick, E., Rezende, D.J., Mohamed, S., Lakshminarayanan, B.: Normalizing flows for probabilistic modeling and inference. *The Journal of Machine Learning Research* **22**(1), 2617–2680 (2021)
- [24] Ridnik, T., Ben-Baruch, E., Noy, A., Zelnik-Manor, L.: Imagenet-21k pretraining for the masses. In: Thirty-fifth Conference on Neural Information Processing Systems Datasets and Benchmarks Track (Round 1) (2021), https://openreview.net/forum?id=Zkj_VcZ6o1
- [25] Roth, K., Pemula, L., Zepeda, J., Schölkopf, B., Brox, T., Gehler, P.: Towards total recall in industrial anomaly detection. In: Proceedings of 2022 IEEE Conference on Computer Vision and Pattern Recognition. pp. 14298–14308 (06 2022). <https://doi.org/10.1109/CVPR52688.2022.01392>
- [26] Rudolph, M., Wandt, B., Rosenhahn, B.: Same same but different: Semi-supervised defect detection with normalizing flows. In: Proceedings of the IEEE/CVF winter conference on applications of computer vision. pp. 1907–1916 (2021)
- [27] Rudolph, M., Wehrbein, T., Rosenhahn, B., Wandt, B.: Asymmetric student-teacher networks for industrial anomaly detection. In: Winter Conference on Applications of Computer Vision (WACV) (Jan 2023)
- [28] Salehi, M., Sadjadi, N., Baselizadeh, S., Rohban, M.H., Rabiee, H.R.: Multiresolution knowledge distillation for anomaly detection. In: Proceedings of the IEEE/CVF conference on computer vision and pattern recognition. pp. 14902–14912 (2021)
- [29] Tien, T.D., Nguyen, A.T., Tran, N.H., Huy, T.D., Duong, S.T., Nguyen, C.D.T., Truong, S.Q.H.: Revisiting reverse distillation for anomaly detection. In: Proceedings of the IEEE/CVF Conference on Computer Vision and Pattern Recognition (CVPR). pp. 24511–24520 (June 2023)
- [30] Vaswani, A., Shazeer, N., Parmar, N., Uszkoreit, J., Jones, L., Gomez, A.N., Kaiser, L.u., Polosukhin, I.: Attention is all you need. In: Guyon, I., Luxburg, U.V., Bengio, S., Wallach, H., Fergus, R., Vishwanathan, S., Garnett, R. (eds.) *Advances in Neural Information Processing Systems*. vol. 30. Curran Associates, Inc. (2017), https://proceedings.neurips.cc/paper_files/paper/2017/file/3f5ee243547dee91fbd053c1c4a845aa-Paper.pdf
- [31] Wang, G., Han, S., Ding, E., Huang, D.: Student-teacher feature pyramid matching for anomaly detection. In: The British Machine Vision Conference (BMVC) (2021)
- [32] Yu, J., Zheng, Y., Wang, X., Li, W., Wu, Y., Zhao, R., Wu, L.: Fastflow: Unsupervised anomaly detection and localization via 2d normalizing flows. *arXiv preprint arXiv:2111.07677* (2021)
- [33] Zhou, Q., Li, W., Jiang, L., Wang, G., Zhou, G., Zhang, S., Zhao, H.: PAD: A dataset and benchmark for pose-agnostic anomaly detection. In: Thirty-seventh Conference on Neural Information Processing Systems Datasets and Benchmarks Track (2023), <https://openreview.net/forum?id=kxFKgqwFNk>
- [34] Zou, Y., Jeong, J., Pemula, L., Zhang, D., Dabeer, O.: Spot-the-difference self-supervised pre-training for anomaly detection and segmentation. *arXiv preprint arXiv:2207.14315* (2022)

A Supplemental material

In this supplemental material, we provide additional quantitative and qualitative results to validate the performance of the proposed approach.

A.1 Ablation on the layers considered for the forward and backward feature transfer networks.

We investigate the impact of transferring features from different levels of the transformer architecture, i.e., layers j and k described in Sec. 3. As shown in Tab. 5, transferring features between layers with high contextualization, i.e., the last four layers, begets better detection and segmentation results, with the transfer between $j = 8$ and $k = 12$ providing the best performance. We also observe that transferring features from closer layers, such as $j = 11$ and $k = 12$, can harm the performance. We believe that being the function learned by a single transformation layer smooth [19], the task of transferring between two close layers is simpler, thus, it might overgeneralize to anomalous samples, leading to worse performance. Conversely, between two farther layers, the function is highly non-linear. Nevertheless, the performance is quite stable after the layer 8, independently of the employed layers.

Table 5: **Layers Ablation.** Best results in **bold**, runner-ups underlined.

Layers	I-AUROC	AUPRO@30%	AUPRO@5%
[1, 4]	0.906	0.828	0.570
[4, 8]	0.940	0.941	0.773
[8, 12]	0.964	0.952	0.787
[10, 12]	<u>0.960</u>	<u>0.950</u>	<u>0.784</u>
[11, 12]	0.956	0.946	0.774

A.2 Ablation on the loss employed to optimize the forward and backward feature transfer networks.

Tab. 6 report the results obtained by the proposed framework considering different losses for the optimization of the forward and backward feature transfer networks, i.e., the Students MLPs. Even though minimizing the cosine distance achieves better performance it is worth noticing that the results are very similar despite the loss function employed.

Table 6: **Loss ablation.** Best results in **bold**, runner-ups underlined.

Loss	I-AUROC	AUPRO@30%	AUPRO@5%
Cosine distance	0.964	0.952	0.787
L2 distance	0.954	0.950	0.786

A.3 Ablation on single contextualization-specific anomaly map.

We present in Tab. 7 the anomaly detection and segmentation results achieved by the proposed methods when considering the single anomaly separately. These results show that by combining anomaly maps from different layers of contextualization we are able to achieve better performance with respect to the single contextualization-specific anomaly maps. Indeed, the combination of multiple maps can be seen as an ensembling of different AD&S models.

A.4 Ablation on different input resolution sizes during training.

We report in Tab. 8 the anomaly detection and segmentation performance achieved by the proposed methods when different input resolution sizes are considered for the feature extractor. The same resolution is used during training and inference, while the evaluation is performed by upsampling

Table 7: **Anomaly map evaluation ablation.** Best results in **bold**, runner-ups underlined.

Anomaly map	I-AUROC	AUPRO@30%	AUPRO@5%
$\Delta_k \cdot \Delta_j$	0.964	0.952	0.787
Δ_j	0.953	0.943	0.773
Δ_k	0.949	0.925	0.745

the output to the original full resolution of the ground-truth. From these results, it is possible to appreciate that the proposed solution is able to exploit the higher resolution and correctly detect and segment the majority of samples, with an I-AUROC of 0.964 at full resolution, compared to 0.899 when providing low-resolution images. The same trend can be observed for the localization metrics, i.e., AUPRO@30% and AUPRO@5%.

Table 8: **Ablation on the input resolution employed at training time.** Best results in **bold**, runner-ups underlined.

Training resolution	I-AUROC	AUPRO@30%	AUPRO@5%
224 × 224	0.899	0.830	0.562
518 × 518	0.952	0.944	0.779
1036 × 1036	0.964	0.952	0.787

A.5 Full results on VisA

For the sake of completeness, in Tab. 9 we report the per-class detection and segmentation performance, previously summarized in Tab. 1 of the main paper. Results are reported for our solution and the state-of-the-art methods on the VisA dataset.

Table 9: **I-AUROC and AUPRO30@% on the VisA dataset for several AD&S methods.** Best results in **bold**, runner-ups underlined. All methods are trained and tested at high-resolution.

	Algorithm	candle	capsules	cashew	chewinggum	fryum	macaroni1	macaroni2	pcb1	pcb2	pcb3	pcb4	pipe_fryum	Mean
I-AUROC	PatchCore [25]	0.986	0.937	0.990	0.991	0.993	0.997	0.934	0.980	0.988	0.996	0.998	0.998	0.982
	SimpleNet [21]	0.964	0.769	0.972	0.984	0.922	0.809	0.618	0.984	0.956	0.949	0.937	0.986	0.904
	EfficientAD [1]	1.000	0.884	0.933	0.996	0.957	0.947	0.967	0.991	0.971	0.972	1.000	1.000	<u>0.968</u>
	RD++ [29]	0.846	0.935	0.862	0.838	0.966	0.964	0.897	0.935	0.972	0.980	0.982	0.990	0.930
	FBFT (Ours)	0.958	0.992	0.972	0.996	0.988	0.931	0.885	0.980	0.938	0.956	0.976	0.999	0.964
AUPRO@30%	PatchCore [25]	0.955	0.575	0.912	0.670	0.836	0.349	0.340	0.941	0.864	0.703	0.910	0.969	0.752
	SimpleNet [21]	0.867	0.574	0.876	0.723	0.766	0.531	0.244	0.801	0.828	0.757	0.737	0.918	0.718
	EfficientAD [1]	0.982	0.897	0.888	0.822	0.895	0.968	0.982	0.945	0.948	0.950	0.982	0.982	<u>0.937</u>
	RD++ [29]	0.964	0.959	0.699	0.642	0.919	0.977	0.979	0.932	0.938	0.957	0.949	0.967	0.907
	FBFT (Ours)	0.979	0.963	0.971	0.908	0.944	0.971	0.961	0.965	0.939	0.910	0.935	0.972	0.952
AUPRO@5%	PatchCore [25]	0.823	0.402	0.783	0.491	0.497	0.140	0.133	0.799	0.609	0.399	0.592	0.831	0.542
	SimpleNet [21]	0.660	0.396	0.650	0.444	0.397	0.221	0.121	0.611	0.579	0.385	0.446	0.715	0.469
	EfficientAD [1]	0.897	0.675	0.715	0.582	0.585	0.839	0.897	0.779	0.775	0.782	0.897	0.897	<u>0.777</u>
	RD++ [29]	0.859	0.826	0.505	0.384	0.749	0.872	0.879	0.789	0.811	0.827	0.739	0.851	0.758
	FBFT (Ours)	0.881	0.833	0.851	0.674	0.751	0.848	0.839	0.834	0.746	0.684	0.664	0.840	0.787

A.6 Training time.

We provide in Tab. 10 the average time needed per class to train every framework given the number of epochs reported in their official implementations. These timings have been computed using the same hardware employed for all our experiments.

A.7 Implementation employed for the competitors and their licenses

For all the competitors [21, 25, 29], except EfficientAD [1], we employed their official implementations. As far as it concerns EfficientAD, which does not provide an official repository, we leverage on an implementation that obtains the most similar results with respect to the values reported in their manuscript [1]. In particular:

- PatchCore: <https://github.com/amazon-science/patchcore-inspection> released under Apache License 2.0;

Table 10: **Training time required on the VisA dataset.** Average training time in hours per class. All methods are trained and tested at high-resolution.

Algorithm	PatchCore [25]	SimpleNet [21]	EfficientAD [1]	RD++ [29]	FBFT (Ours)
Training time	1.212	6.266	7.783	28.767	2.361

- SimpleNet: <https://github.com/DonaldRR/SimpleNet> released under MIT License;
- RD++: <https://github.com/tientrandinh/Revisiting-Reverse-Distillation> released under MIT License;
- EfficientAD: <https://github.com/nelson1425/EfficientAD> released under Apache License 2.0.

A.8 License for the employed datasets

The VisA dataset [34] is released under the Creative Commons Attribution (CC BY 4.0) license. The MVTec AD dataset [4] is released under the Creative Commons Attribution-NonCommercial-ShareAlike 4.0 International License (CC BY-NC-SA 4.0).

A.9 Additional qualitative results on the VisA and MVTec AD datasets.

As anticipated in the main paper, we show in Fig. 7 some additional qualitative results for the remaining classes of the VisA dataset which have not been reported in Fig. 5. As already highlighted in Sec. 5, the anomaly maps produced by our solution provide a more localized response for the anomalies, compared to EfficientAD [1].

Additionally, in Fig. 8 we show some qualitative examples of the anomaly map produced by our model on the MVTec AD dataset. Also in this scenario, our method provides more localized anomaly scores, motivating the segmentation performance gap in terms of both AUPRO@30% and AUPRO@5%.

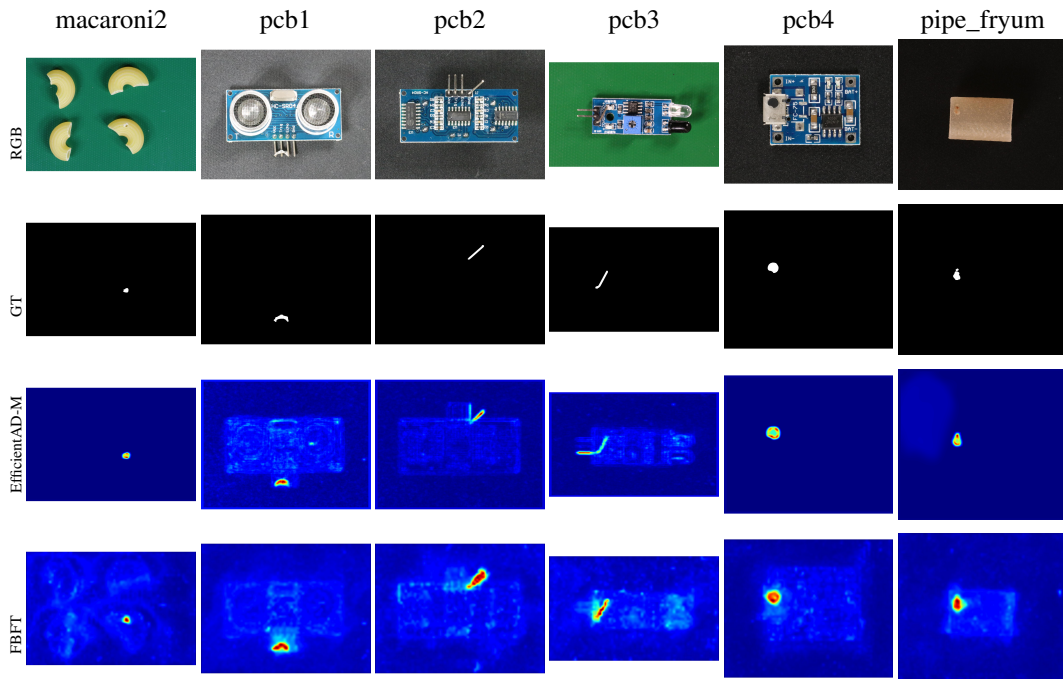


Figure 7: **VisA dataset qualitative results.** All methods are trained and tested at high resolution.

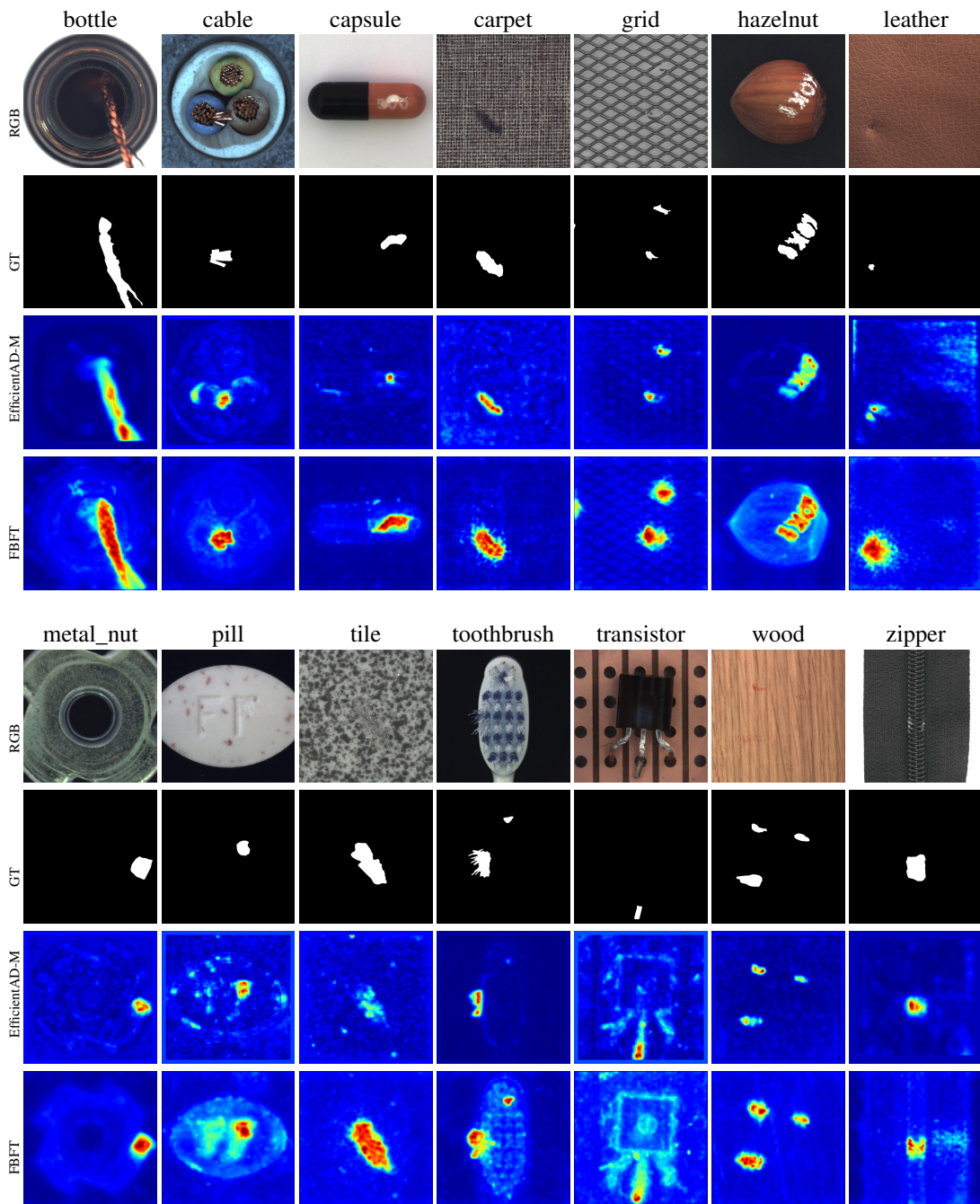


Figure 8: MVTec AD dataset qualitative results.